Single Photon Imaging X-ray Spectrometers

K. Segall, C.M. Wilson, L. Li, A.K. Davies, R. Lathrop, M.C. Gaidis, D.E. Prober
Yale University, Department of Applied Physics, New Haven, Connecticut 06520-8284

A.E. Szymkowiak and S.H. Moseley
NASA Goddard Space Flight Center, Greenbelt, Maryland 20771

***Abstract*—We have developed superconducting, single-photon imaging x-ray detectors with an energy resolution of 26 eV FWHM at 6 keV and a spatial resolution of 0.5 μm over an effective area of 18 μm x 100 μm. The energy resolution is among the best reported for this kind of detector and is within a factor of ≈ 4 of it's theoretical limit. The calculated absorption efficiency of the detector is 28%. Scaling to larger areas and higher quantum efficiency appear possible. We discuss the device design and readout along with possible sources of resolution broadening.**

I. Introduction

Superconducting Tunnel Junctions (STJs) are being investigated by several groups for use as single photon, non-dispersive spectrometers at a wide range of photon energies. A photon absorbed in a superconducting film creates excess quasiparticles, the number of which is proportional to the photon energy. If an STJ is attached to the absorbing film, the excess quasiparticles can tunnel through the insulating barrier and cause an increase in the junction's subgap current. The integral of the increase in current, the charge, is proportional to the number of quasiparticles created and thus provides a measure of the photon energy. The accuracy of this type of measurement is limited by statistical fluctuations in the number of quasiparticles created. Because of the small excitation energy (≈ 2Δ) in the superconducting absorber, these devices have an excellent theoretical energy resolution for x-rays, less than 10 eV full width at half maximum (FWHM) for a photon energy of 6 keV using a tantalum superconducting absorber. The theoretical limit for energy resolution has been approached by two groups [1]-[3] at a few different values of photon energies, with [1] reporting the best value for the 6 keV line, 22eV FWHM over an area of ≈ 75 μm^2.

Applications for these type of detectors are expected in several areas, including x-ray astrophysics. Hot gaseous plasmas and supernova remnants show thermal and line emission in the soft x-ray region (0.1-10 keV), with elemental lines spaced approximately 10 eV apart. High energy resolution (≈ 10 eV) is needed to resolve the ionization states and to study density and kinematics, yet is not available in existing semiconducting detectors such as x-ray CCDs. STJs can potentially provide the needed energy resolution, large collecting area and high quantum efficiency. Many applications also require spatial resolution in order to image spatially extended objects. Astrophysical observations are made from satellites and rockets where an imaging, photon counting detector can be used to relax the pointing requirements of the spacecraft. Since power consumption and complexity are issues for rocket and satellite experiments, especially with sub-Kelvin detectors, it is also desirable to have as few readout channels as possible.

We are developing superconducting Nb-Ta-Al-AlOx-Al tunnel junction detectors for astrophysical applications. The devices utilize a lateral double junction geometry which has inherent 1-D spatial imaging with only 2 channels of readout. The device studied has an active area of 160 μm x 100 μm and a calculated quantum efficiency of 28% at 6 keV. Both of these figures can be improved. In addition, under select circumstances the device displays excellent energy resolution, 26 eV FWHM at 6 keV, among the best reported for this kind of detector. We discuss contributions to the spectral and spatial resolution along with scaling to larger device areas.

II. Device Geometry and Electronic Readout

The two junction geometry is shown in Fig. 1. A Ta film (Δ_{Ta} = 0.7 meV) 200μm x 100 μm x 600 nm thick forms the superconducting absorber. At 6 keV, 600 nm thickness of Ta absorbs about 28% of incident x-rays; future devices should be able to utilize thicker films. Note that in contrast to vertical stacked devices, there is no Ta under the tunnel junction which might affect or limit the quality of the junction. A thin strip of Nb (Δ_{nb} = 1.5 meV) makes

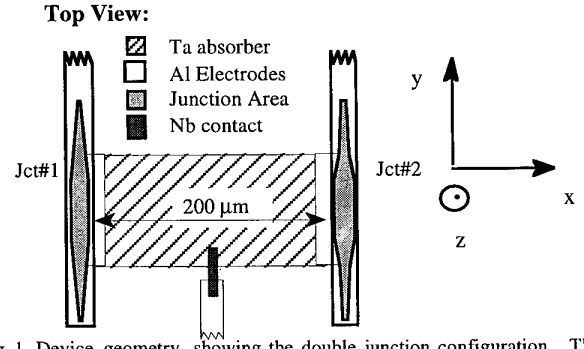

Fig. 1. Device geometry, showing the double junction configuration. The Al electrodes overlap the tantalum absorber by 10 μm on each side.

Manuscript received September 15, 1998.
This work was supported by NASA Grant No. NAG5-2892

1051-8223/99$10.00 © 1999 IEEE

electrical contact to the center of the absorber. The readout is formed by two Al-AlOx-Al junctions, one on either side, which overlap the Ta by 10 μm. The device fabrication procedures have been published elsewhere [4]. X-rays absorbed in the Ta break Cooper pairs and create excess quasiparticles, which cool quickly to near the gap edge. They then diffuse to either side, and after reaching one of the two Al regions (traps) they scatter inelastically toward the Al gap energy (Δ_{Al} = 0.18 meV) and become confined to the region close to the tunnel barrier. The quasiparticles then tunnel across the barrier to the counterelectrode. The charge separation into two readout junctions allows for inherent spatial resolution [5], as the ratio of the charge collected at each junction can be used to infer the photon absorption location in one dimension.

The devices are biased and read out with a low noise current preamplifier. A small magnetic field (≈ 15 Gauss) is applied parallel to the film to suppress the DC Josephson current in order to allow biasing in the subgap region. We use a DC voltage bias, which is preferable to DC current bias because it prevents the junction from temporarily switching to zero voltage if the DC Josephson current cannot be completely suppressed at a single value of applied magnetic field. The circuit also provides the low noise current preamplifier for the pulse readout. A current amplifier is chosen because the current waveforms are directly related to the time-dependent processes inside the device [6]; the charge is determined by numerical integration in a later step. The preamplifier has a current noise of 0.25 pA/√Hz, a voltage noise of 0.5 nV/√Hz and a bandwidth of ≈ 100 kHz. Details of the circuit design and performance have been published [7].

III. Spectral and Spatial Resolution

The device was cooled down and operated at a temperature of 0.21 K in a two stage ^{3}He cryostat. At a typical bias point of 70 μV the bias current is 25 nA and the quiescent differential resistance is 15-20 kΩ. We illuminate the device with an ^{55}Fe x-ray source that emits two Mn lines at 5.89 keV (K_α) and 6.49 keV (K_β). We digitize and record the entire unfiltered waveforms on disk, and later apply digital filters to the current waveforms and numerically integrate them to obtain the charge from each junction. With no quasiparticle loss in the absorber a plot of the charge from the two junctions, Q_1 vs. Q_2, would be a straight line for fixed photon energy. A typical plot of Q_1 vs. Q_2 is shown in Fig. 2. The curvature in the plot indicates quasiparticle losses in the absorber, since quasiparticles created in the center of the device have to diffuse a longer distance (time) before being trapped in either junction. Later we discuss the implications of the losses for scaling to larger absorber sizes; measurements of the loss time and diffusion constant have already been published [6]. One can model the charge output assuming a constant quasiparticle loss rate [5], extract the total initial charge after correction for loss (Q_{total}) and display

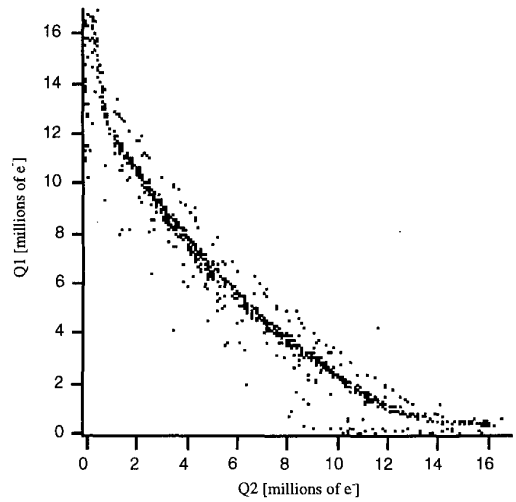

Fig. 2. Charge collected in junction 1 vs. charge collected in junction 2. The data have not been filtered. The curvature in the plot is due to quasiparticles lost to recombination as they diffuse to the junctions.

it as a function of absorption location. Fig. 3 shows the data from Fig. 2 displayed in this way after filtering with a digital 4th order 3.4 to 40 kHz Chebyshev filter. The filter reduces the total charge but maximizes the signal-to-noise ratio.

The plot in Fig. 3 shows several interesting features. The two lines, the stronger K_α and the weaker K_β, are evident at Q_{total} = 6.14 and 6.73 million electrons. The collected charge for the two lines is in the ratio of the line energies to within 1%, showing good linearity over that range. The total collected charge increases in the last 10-20 μm of either side, where the Al trap overlaps the Ta absorber. In these regions the average energy gap is lower than in the bulk Ta, due to the proximity effect; absorption events in these regions thus create more charge. In addition, the variation of the charge is much larger for events in the center of the device. The exact

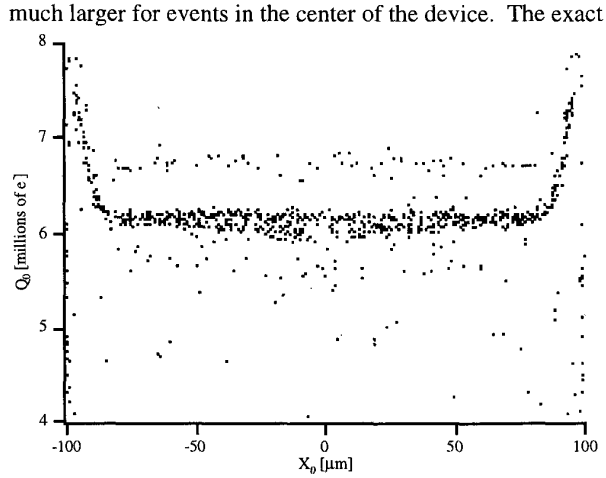

Fig. 3. Total charge (Q_0), after correction for losses, vs. absorption location (X_0). The data have been filtered. The K_α line is located at 6.14 million electrons and the K_β line at 6.73 million electrons. The magnitude of Q_0 increases near the ends where the Al overlaps the Ta.

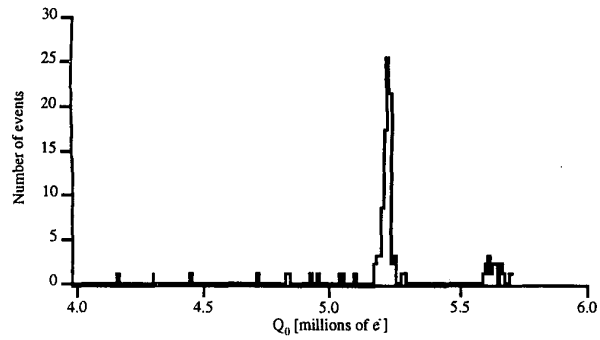

Fig. 4. Histogram of collected charge, over an 18 μm x 100 μm range. The width of the distribution is 26 eV FWHM.

cause of this excess broadening is not known, but is believed to be related to quasiparticle loss at the Nb contact (see discussion below).

The energy resolution of the device is determined by measuring the width of the distribution of the total charges in a histogram. Excluding the last 20 μm of the device on either side, the energy resolution for the remaining 160 μm is 80-90 eV FWHM. However, the resolution is much better over a smaller section of the device, away from the Nb contact. The best resolution obtained was for an 18 μm range, from +67 μm to +85 μm. Fig. 4 shows a histogram of the total charge, filtered with the same filter as Fig.3 (data in Fig.4 is the same device but from a different cryogenic run than from Fig. 2 and 3). Note that there is no "double peak" structure as in vertically stacked devices. A Gaussian fit to the data gives a resolution of 26 eV FWHM. In looking at a smaller section of the total device area we have reduced the total number of counts in the histogram to ≈ 100, thus giving a statistical error of $\sqrt{N}/N \approx 10$ % in the resolution.

The essential feature of our detectors is the combination of high spectral and spatial resolution. The spatial resolution is expected to be of the same order as the energy resolution, i.e. 0.5-1.5%. To properly measure the spatial resolution would require confining the illumination to a "point" spot, much smaller than the expected broadening. We have not done such a measurement, but we can estimate the spatial resolution from the energy resolution by propagation of errors [5]. An energy resolution of 85 eV, across a 160 μm range, would imply a spatial resolution of 2 μm, thus providing 80 pixels with just two channels of readout. For an energy resolution of 26 eV, if obtained for the full 160 μm length, the spatial resolution would be 0.5 μm (320 pixels).

IV. Noise Sources

To make the detector truly useful for x-ray astronomy it is necessary to reduce the resolution to near the theoretical limit, ≈ 6 eV FWHM for the device previously discussed. The 26 eV measured so far is thus dominated by extraneous noise sources. We discuss three possible contributions to the broadening: (1) spatial noise, a variation of the signal caused by absorption at different spatial locations in the device; (2) bias voltage fluctuations, a variation of the signal due to pulse-to-pulse differences in the bias voltage, which affect the gain of the device; and (3) electronic noise, broadening due to the current and voltage noise of the electronic readout. It is our belief that these sources contribute the majority of the excess broadening, and that elimination of these sources will bring the resolution to near the theoretical limit.

As mentioned previously, the spatial noise is believed to result from quasiparticle loss at the Nb contact. Niobium is used because its large energy gap should prevent quasiparticles from diffusing into the leads. However, Nb is also known to produce metallic suboxides, which may form local trapping sites on the surface of the Ta. Quasiparticles that are trapped at these sites would eventually recombine rather than tunnel. This would cause a dependence of the total charge on the y-location of the absorption position (see Fig. 1 for orientation). Absorption events which occur toward the bottom of the figure (in y-direction), nearer to the contact, would suffer more loss of charge than absorption events which occur near the top of the figure, away from the contact. This effect would be more pronounced for events in the center of the device (in x direction), and would thus give rise to data similar to Fig. 3. It is believed that, by looking only at events away from the center, we do not see the effects of this noise source, i.e. it does not contribute significantly to the 26 eV previously mentioned. However, it does dominate the resolution when looking at the full absorber, and therefore future devices must avoid this problem. We have designed devices which do not use Nb, but rather use a thin Ta contact or a Ta contact to the Al trap instead. These devices are currently being fabricated.

The dependence of the total charge on bias voltage can be understood from the I-V curve during an x-ray pulse. Fig. 5 shows a schematic of the I-V curve in the quiescent state (no x-ray) and the dynamic state (during an x-ray pulse). The

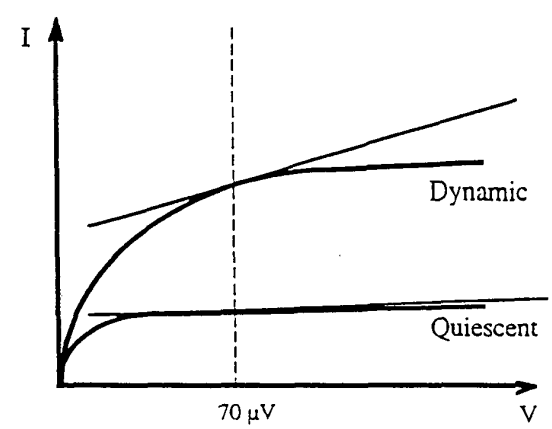

Fig. 5. Schematic of the I-V curve in the quiescent state (no photon) and dynamic state (with photon). The slope of the curve, dI/dV (differential conductance), is higher in the dynamic state. This also results in a bias dependence of the collected charge.

curve in the dynamic state is our estimate of the behavior. It has a larger slope than the quiescent curve because during the pulse the excitations in the junction are at a temperature T_{eff} which is greater than T_{bath}. The larger slope during the pulse implies that the current depends much more on the voltage than for the quiescent curve.

The reason that T_{eff} is greater than T_{bath} is as follows. After an x-ray is absorbed in the Ta, the quasiparticles relax very quickly to near the gap edge. They diffuse in Ta to the Al trap region where they then scatter down toward the Al gap. In the Al trap, however, the quasiparticles do not scatter to near the gap edge as in Ta because the scattering times in Al are much longer than in Ta [8]. When the quasiparticles tunnel, therefore, they are at a much higher effective temperature than the bath. We estimate $T_{eff} \approx 1K$. Thus in the dynamic state the current, and also the charge, are increasing functions of voltage. In addition, the differential resistance (dV/dI) is reduced from its quiescent value, which affects the electronic noise (see below). A plot of Q_{total} vs. bias voltage is given in [6]; the shape is almost identical to that of the dynamic I-V curve drawn schematically in Fig.5. From a fit to the Q_{total} vs. V_{bias} curve we can estimate that a 1 μV change in bias voltage results in a 40 eV change in signal. An estimate of how stable the bias voltage is in our circuit is approximately 150 nV rms, corresponding to a broadening of ≈ 14 eV FWHM.

The last source of noise we consider is electronic noise. In a separate measurement, we bias the detector at a typical bias point and inject electronic current pulses into the amplifier to measure the noise contribution of the amplifier alone. We apply filters, integrate the current numerically, and bin them in a histogram in identical fashion to the x-ray experiment. This experiment yields a resolution of 15 ± 3 eV FWHM. The dominant contributions to the electronic noise come from (1) the Johnson current noise of the feedback resistor, (2) the shot noise of the junction bias current, and (3) the current noise due to the voltage noise of the input FET, which appears proportional to $(dV/dI)^{-1}$[6]. The last term is higher in the dynamic state than in the quiescent state due to the reduced dynamic resistance (dV/dI) during a pulse. A true measurement of the electronic noise during a pulse is difficult. A good estimate of the differential resistance during a pulse is 2 kΩ (reduced from ≈ 15 kΩ), which would cause the electronic noise to be 21 eV in the dynamic state. The sum of all the noise contributions is given in Table 1. With the exception of the statistical limit, which is calculated from theory, all other noise values are estimated. The noises add in quadrature to match the measured values of total noise. The dynamic value of 21 eV (instead of the measured 15 eV) is used for the electronic noise in this sum.

We now consider scaling to larger (i.e., longer) devices. Since the electronic noise should not scale with signal size, the drop in signal amplitude due to increased losses in a longer absorber corresponds to a degradation of the resolution. This puts a cost to scaling to larger device sizes. To be useful for x-ray astronomy, absorber sizes of order 1 mm are needed. Assuming the same loss *rate*, a 1 mm-long device would have more *total* loss. This will reduce the signal in a 1 mm-long device. Therefore, an electronic noise equivalent to 1 eV FWHM in the existing device would be required to maintain the total noise of 26 eV FWHM in a 1 mm-long device. This should be possible with a cold feedback resistor, a lower operating temperature and smaller tunnel junctions [7].

TABLE I: ESTIMATED NOISE CONTRIBUTIONS FROM THE FULL ABSORBER (ΔE_{ABS}) AND FROM THE SELECTED RANGE (ΔE_{SEL}).

Noise Source	ΔE_{Abs}	ΔE_{Sel}
Spatial Noise	86 eV	< 5 eV
Bias Fluctuations	14 eV	14 eV
Electronic Noise (measured)	21 eV (15 eV)	21 eV (15 eV)
Statistical Limit	6 eV	6 eV
TOTAL:	**90 eV**	**26 eV**

V. SUMMARY

We have developed superconducting, single-photon imaging spectrometers. The measured device energy resolution, 26 eV FWHM over an 18 μm x 100 μm range, is among the best reported for this kind of detector. The device also displays inherent imaging capabilities, 0.5 μm spatial resolution over the same area. Modest improvements in the energy resolution, quantum efficiency and active area appear possible and should make the device useful for applications in x-ray astrophysics.

ACKNOWLEDGMENT

We thank R.G. Wheeler, P.J. Kindlmann, S. Friedrich, D.Schiminovich and F.S. Porter for useful discussion. Devices were fabricated by M.C. Gaidis.

REFERENCES

[1] P. Verhoeve, N. Rando, A. Peacock, A. van Dordrecht, B.G. Taylor, and D.J. Goldie, *Appl. Phys. Lett.*, vol. 72, pp. 3359-3361, 1998.

[2] J.B. le Grand et al., *Appl. Phys. Lett.*, vol. 73, pp. 1295-1297, 1998.

[3] P. Verhoeve, N. Rando, A. Peacock, A. van Dordrecht, and A. Poelaert, *IEEE Trans. Appl. Supercond.*, vol. 7, p. 3359, 1997.

[4] M.C. Gaidis et al., *IEEE Trans. Appl. Supercond.*, vol. 6, pp. 1-4, 1996.

[5] H. Kraus, F.V. Freilitzsch, J. Jochum, R.L. Mossbauer, T. Peterreins, and F. Probst, *Phys. Lett. B*, vol. 321, p. 195, 1989.

[6] S. Friedrich et al., *Appl. Phys. Lett.*, vol. 71, pp. 3901-3903, 1997.

[7] S. Friedrich et al., *IEEE Trans. Appl. Supercond.*, vol. 7, pp. 3383-3386, 1997.

[8] S.B. Kaplan, C.C. Chi, D.N. Langenberg, J.J. Chang, S. Jafarey, and D.J. Scalpino, *Phys. Rev. B*, vol. 14, p. 4854, 1976.